Title	Damage and permeability in tape-laid theromplastic composite cryogenic tanks.
Author(s)	Grogan, David M.; Ó Brádaigh, Conchúr M.; McGarry, J. P.; Leen, Sean B.
Publication Date	2015-09-07
Publication Information	Grogan, D.M., Ó Brádaigh, C.M., McGarry, J.P., Leen, S.B. (2015) 'Damage and permeability in tape-laid theromplastic composite cryogenic tanks'. Composites Part A-Applied Science And Manufacturing, 78 :390-402.
Link to publisher's version	http://dx.doi.org/10.1016/j.compositesa.2015.08.037
Item record	http://hdl.handle.net/10379/5406
DOI	http://dx.doi.org/10.1016/j.compositesa.2015.08.037

Damage and permeability in tape-laid thermoplastic composite cryogenic tanks

D.M. Grogan[1*], C.M. Ó Brádaigh[2], J.P. McGarry[1], S.B. Leen[1]

[1]*Mechanical Engineering, National University of Ireland, Galway, Ireland*

[2]*MaREI Centre, School of Engineering, University College Cork, Ireland*

Abstract

This work presents a combined experimental and numerical approach to the design and analysis of tape-laid thermoplastic composite cryogenic tanks. A detailed material and defect characterisation of automated tape-laid CF/PEEK is undertaken using optical micrography and 3D X-ray CT (computed tomography) as well as cryogenic testing to investigate damage formation. Resulting material data is used as input for a novel XFEM (extended finite element method)-cohesive zone methodology which is used to predict intra- and inter-ply damage in an internally pressurised cryogenic tank. An optimised tank lay-up is presented and analysed using the numerical method to ensure resistance to microcrack formation and fuel leakage through the tanks walls under operating loads.

* **Corresponding author email: d.grogan1@nuigalway.ie. Phone: +353876155026**

1. Introduction

Due to their high specific strength and stiffness amongst other properties, carbon-fibre reinforced polymers (CFRP) are seen as candidate materials for the fuel tanks of next generation reusable launch vehicles (RLVs). These fuel tanks will be exposed to cryogenic temperatures as low as -250 °C and to internal pressurisation as high as 1 MPa. This extreme thermo-mechanical loading can lead to microcracking and delamination formation within the CFRP, which, in severe cases, can result in permeation of the cryogen through the fuel tank walls. A precise understanding, therefore, of the methods of damage accumulation in the material and how the various damage modes interact underpins the potential use of CFRP for RLVs.

While numerous works have been published on the design and testing of composite overwrapped pressure vessels (COPVs) [1-4], the unique challenges posed by cryogenic fuel storage have yet to be fully addressed. Work on the design and analysis of composite cryo-tanks has intensified since the failure of the NASA/Lockheed X-33 RLV fuel tank [5], where fuel leakage occurred due to cryogenically induced damage in the composite tank wall. Subsequent experimental and theoretical analyses of cryo-tanks [6, 7] have found that, unlike traditional COPVs, the thermal stresses induced by cryogenic loading are the main design consideration and play a critical role in damage formation. In addition, the role of material quality and processing conditions on damage initiation remain understudied [8, 9], particularly for advanced thermoplastic composites such as CF/PEEK, which are increasingly used in conjunction with novel processing techniques such as automated tape laying (ATL) for the manufacturing of large structures.

Thermoplastic composites offer several advantages over thermosets in terms of their improved range of properties and processing techniques available. CF/PEEK is a high-performance thermoplastic carbon-composite material, which is increasingly being used in the aerospace industry for weight sensitive designs and is also known to offer increased resistance to damage propagation compared to epoxy based materials [10, 11]. Importantly, thermoplastics allow the use of out-of-autoclave processing techniques such as automated tape laying (ATL), a relatively new processing method based on the in-situ consolidation of plies. This is carried out by a computer controlled robot which typically applies pre-preg tape to a heated mould placed on a revolving mandrel, using a heat source such as a laser which is focused on the ply lay-down area. Unlike autoclave processing, consolidation occurs at the point where the robotic head first heats, then melts and finally consolidates and cools the incoming tape, as opposed to

2

processing the entire laminate simultaneously. This facilitates the manufacture of large structures without the investment required for a large autoclave of several metres diameter. Thus the technique is well suited to producing components such as cryo-tanks. The main drawbacks of this technique include the potential for poor ply adhesion due to insufficient melting and adhesion and the presence of significant residual stress gradients due to non-uniform cooling [8, 12, 13]. The tape- laying process itself can also result in gaps due to overlapping plies which can result in high void contents. These issues can often lead to composite laminates of a lower general quality than those produced in an autoclave [9, 14].

CF/PEEK, due to its high processing temperature and semi-crystalline nature, exhibits significant property variation with temperature. Residual stress build-up for CF/PEEK laminates begins below the stress free temperature (SFT), which is approximately 315 °C [15]. This is far above the glass transition temperature of 143 °C, which usually marks the point of residual stress formation for amorphous polymeric composites. Thus, using this material for cryogenic applications can involve having to design for thermal residual stresses due to temperature changes in excess of 500 °C. The difficulty in accurately characterising material properties over such a wide temperature range means that little experimental data is available from the literature, particularly for relatively novel materials such as tape-laid CF/PEEK.

This work aims to advance the design and analysis of linerless composite cryo-tanks by combining the extensive material characterisation of a tape-laid composite with a novel numerical methodology capable of predicting composite laminate damage and permeability. This approach represents a significant departure from existing analysis methods such as unit cell, first-ply-failure and continuum analyses [6, 16-21] by allowing the discrete damage modelling of large structures using detailed material data inputs. An optimised cryo-tank design is also presented, which accounts for the thermo-mechanical stresses resulting from processing, fuelling and internal pressurisation. A sub-model meso-scale damage analysis shows that the optimised tank design is capable of preventing fuel leakage after exposure to cryogenic temperatures and internal pressurisation.

2. Material characterisation

2.1 Overview of material properties

Measurements of temperature-dependant mechanical, thermal and fracture properties of CF/PEEK materials have been collated from several sources in tables 1 and 2. Using the properties of the tape laid Suprem IM7 [22] at 25 °C from table 1 as a base, temperature-dependant data is generated by

3

interpolation and normalisation using fitting functions across a range of temperatures for available material data. Table 3 presents the resulting interpolated temperature dependant data which is used in subsequent modelling work, described in Section 3.

When compared with previously published material data for a similar grade of CF/PEEK processed using an autoclave [26], the tape-laid material exhibits lower strength values, particularly in the matrix-dominated directions. Transverse tensile strength alone was found to reduce by a third for the tape laid material. The increased presence of manufacturing defects resulting from the tape-laying process contributes to this property degradation.

2.2 Defect characterisation

The void and inclusion content for several types of tape-laid CF/PEEK laminates were measured using 3D X-ray computed tomography (CT). This non-destructive testing technique allows full internal characterisation of a specimen based on the varying densities of its constitutive material phases. The specimens (see Table 4) were manufactured from a Suprem T/60%/IM7/PEEK/150 material with 0.14 mm ply thickness and included:

- Two unidirectional coupons, named UD1 and UD2 from a flat plate (16 ply, 34 mm × 27 mm)
- Two [45°/-45°/90°/0°/90°/0°/90°/0°/90°]$_S$ coupons QI1 and QI2, from a flat plate (18-ply, 34 mm × 27 mm)
- One Unidirectional hoop wound section (16-ply, 500 mm diameter)

A KUKA KR 180 R2900 robot with a laser-line diode laser module (LDM) 3000W system operated by the Irish Centre for Composites Research (ICOMP) and based at the University of Limerick [14], Ireland, was used to manufacture the specimens. The nominal process parameters included a lay-down speed of 6m/min, a target temperature of 420 °C, a tool temperature of 280 °C, a roller pressure supply of 4.5 bar. and a laser power of 500 W.

The CT scans were carried out using a *Phoenix M nano/microtom* at a scan resolution of 33 μm. The X-ray gun was rated at 180 kV, with scans being carried out at 160 kV and 28 μA, giving a scan power of 4.5 W. A total of 1,000 images were generated for each scan over a 360° field of view, for a total scan time of 67 minutes. The tomographical reconstruction was carried out using *Davos* software, whilst

4

volume rendering was completed using *VGStudio MAX 2.2*. Fig. 1 shows a rendered CT scan of voids in the UD1 and hoop specimens.

Complete characterisation of individual void morphology and total void volume content within the scan area is possible using this technique. Table 4 provides details of the average x, y and z dimensions of the voids ($\bar{x}$, $\bar{y}$, $\bar{z}$) and their respective standard deviations ($\sigma(x)$, $\sigma(y)$, $\sigma(z)$) for each specimen type as measured using the volume-rendering software. The total void volume as a percentage of the specimen volume is also provided.

Although all specimens were found to have a void volume content below the 1.5% considered generally acceptable for aerospace components, they compared relatively poorly with similar autoclaved specimens which were found to have an order of magnitude lower void contents [28]. The unidirectional and hoop specimens were found to have lower void contents, likely due to the absence of air gaps, which are discussed in Section 2.3. As expected, the void geometry was found to be related to the laminate lay-up, with the largest dimension of the voids being aligned with the fibre direction (x) and the smallest dimension being in the thickness direction (z). This trend also carried through to the computed standard deviations of the void dimensions. The specimen QI2 was found to have a particularily high void content due to a large number of gaps being present, which in turn skewed the measured void morphology. A more detailed overview of void morphology for the UD1 and QI1 specimens is provided in Fig. 2. Fig. 2 (a) and (b), which show the distribution of void volumes within the specimens. The vast majority of voids have a volume of less than 0.05 mm^3, although a large proportion of the total void volume is contained within a minority of large voids. This is particularily true for the QI1 specimen, where less than 10% of voids account for 64% of the total void volume. Fig. 2 (c) shows the relationship between void sphericity and void radius, where sphericity is defined as the ratio between the surface of a sphere with the same volume as the defect and the surface of the defect. Smaller voids tend to be more spherical while larger voids are more elongated and elliptical. It should be noted that inclusion content for all specimens was found to be negligible.

2.3 Microcracking and gaps

The specimens were also examined for the presence of microcracks and gaps, which can arise due to processing. One side of each of the UD and QI specimens was polished to facilitate optical examination under a microscope. No microcracks or gaps were observed in the UD specimens. Minor damage was

5

detected in the QI1 and QI2 specimens as-processed in the form of 3 surface microcracks across all polished surfaces. Six gaps were detected in the QI1 specimen and seven in the QI2 specimen, with QI2 containing several notably wide gaps, as can be seen in Fig. 3. The QI1 and QI2 specimens were also exposed to a single cryogenic cycle via immersion in liquid nitrogen (LN_2) from -196 °C to 40 °C in order to examine the resulting damage formation and its implications for laminate permeability.

Moderate damage accumulation was observed post-cycling with transverse microcracks forming in the outer and central plies as shown in Fig. 4 (a), although the presence of through-thickness crack networks was not obvious. However, the location of gaps in otherwise un-damaged plies led to a reduction in the number of pristine barrier plies, with the consequence of decreased resistance to leakage if the material was used for a cryo-tank. Average crack opening displacement (COD), shown in Fig. 4 (b), was found to be relatively low when compared to previous work [28]. This is due to the constantly varying ply orientation and lack of ply blocking. Although the likelihood of through-thickness crack networks forming in the laminates is greatly increased by the presence of gaps, which themselves can be over 100 times the width of microcracks, their presence can be significantly reduced by appropriate adjustment of the tape placement width.

3. Cryo-tank modelling

3.1 Tank design

Aside from external launch and structural loads, the primary design considerations for cryo-tanks for space applications are temperature and pressure based. Unlike conventional composite overwrapped pressure vessels (COPVs), which require a liner to prevent fluid leakage [29], linerless composite tanks must remain impermeable without the presence of additional barrier materials. Additionally, due to the large temperature difference between processing temperatures and the cryogenic fuel, thermal loading is the dominant load form. Internal tank pressure is generally far below the levels that typical COPV designs can tolerate. For this reason, mitigation of thermal stress is seen as a key design requirement for linerless cryo-tanks.

In this work, a design for a scaled-down version of a cryo-tank for a RLV is presented. The tank has a 500 mm diameter and holds approximately 90 litres of cryogen. A symmetric 20-ply lay-up, giving a wall thickness of 2.8 mm, is used. This is in order to ensure structural integrity at a maximum expected operating pressure of 10 bar. Both material processing and tank fuelling are represented by a two-stage

6

thermal load as shown in Fig. 5. This is due to the residual stress formation which can occur in thermoplastic laminates from the SFT to ambient temperature. Different convection coefficients (h) are used to simulate the rate of cooling for each stage, with significantly more severe thermal gradients associated with the fuelling stage than the processing stage.

The design of the tank lay-up is key to preventing damage formation and leakage. Assuming a leak-before-burst criterion focused on the cylindrical portion of the tank (Fig. 6), the following steps were adopted in designing the general stacking sequence:

1. Limiting of thermal stress is prioritised due to the large temperature change. Therefore ply-angle variation is minimised throughout the lay-up. A unidirectional lay-up is most suited for the reduction of laminate level thermal stress, but is not practical for resisting internal pressurisation loads.

2. For an internally-pressurised tank with closed ends, the nominal hoop stress is twice the axial stress. Therefore an optimal unidirectional lay-up should have the fibres orientated in the hoop direction.

3. The axial stress due to internal pressure then becomes the limiting design failure issue due to the possibility of transverse failure of the hoop-orientated plies.

4. This axial stress is reduced by rotating the angles of specific hoop plies towards the axial direction. This must be designed to also balance with increasing thermal stresses due to the increasing ply-angle variation.

The wound composite modeller (WCM) [30], a plugin for Abaqus FEA software, was used to rapidly test prospective lay-ups based on the latter design steps. As is the case with conventional filament winding methods, plies were grouped in opposing pairs according to the following general lay-up: $[90°_2/\pm\theta°/\pm\theta°/90°_2/\pm\theta°_2]_S$. Fig. 7 shows the predicted stress distributions transverse to the fibre direction through the cylindrical portion of the tank wall for several lay-up iterations at maximum expected operating loads.

Ensuring that the transverse tensile strength of the composite is not exceeded is an important factor in limiting matrix microcracking and hence leakage. Fig. 7 shows a clear trend in the relationship between decreasing ply angle variation and decreasing peak transverse stress. Conventional COPV lay-ups using a mixture of hoop and low-angle helical plies (plies between 5° and 30°) are shown to be unsuitable for the unique demands of cryogenic fuel storage, where the minimisation of thermal stress is critical. As the

7

[90°$_2$/±75°/±75°/90°$_2$/±60°$_2$]$_S$ lay-up was the only stacking sequence in which the transverse strength of the composite was not exceeded in every ply, it was selected for more in-depth analysis via the damage sub-model outlined below in Section 3.2. It should be noted that for certain conventional filament winding methods, such a high-angle helical lay-up would not enable full coverage of the polar boss regions around the ends of the tank. Additional reinforcement in the form of pre-fabricated doilies [1, 31] would be required at the polar bosses in order to ensure continuation of the desired lay-up from the cylindrical section to the dome section of the tank.

3.2 Combined XFEM-SCZM damage method

A combined XFEM (extended finite element method) and SCZM (surface cohesive zone model) approach to damage modelling in composite laminates is developed here. Modelling is focused on the meso-scale, with XFEM being used for microcrack initiation and propagation (intra-laminar failure) and SCZM for mixed-mode delamination growth between plies (inter-laminar failure). This methodology allows the discrete modelling of microcracks and hence prediction of laminate permeability. It is also applicable to relatively large-scale structures such as cryo-tanks (Fig. 8). The general XFEM-SCZM approach is implemented within an adapted form of the general purpose, non-linear finite element code, *Abaqus v6.14*, as is described in detail in previous work [32, 33].

However, due to the complex thermo-mechanical load state present in the cryo-tank, the original method [33] has been improved here to incorporate a more sophisticated mixed-mode compression-shear matrix failure criterion. Oblique fracture planes aligned with the fibre angle are now permitted, along with the usual transverse microcracking perpendicular to the ply interface. Fig. 9 illustrates the main matrix failure modes modelled using XFEM for an assumed two-element model.

This enhancement is implemented through a user defined damage initiation sub-routine (UDMGINI) [34] within the general XFEM framework. A crack is assumed to initiate when the relevant fracture criterion, f, is exceeded, where f_t is the tensile failure criterion and f_c is the compressive failure criterion. This criterion is based on the Hashin failure criteria [35] for matrix failure:

- For tensile matrix failure ($\sigma_{22} + \sigma_{33} > 0$), $f_t \geq 1 =$ failure

$$f_t = \frac{(\sigma_{22}+\sigma_{33})^2}{Y_T^2} + \frac{\sigma_{23}^2 - \sigma_{22}\sigma_{33}}{S_{23}^2} + \frac{\sigma_{12}^2 + \sigma_{13}^2}{S_{12}^2} \qquad (1)$$

8

- For compressive matrix failure ($\sigma_{22} + \sigma_{33} < 0$), $f_c \geq 1 =$ failure

$$f_c = \left[\left(\frac{Y_C}{2S_{23}}\right)^2 - 1\right]\left(\frac{\sigma_{22}+\sigma_{33}}{Y_C}\right) + \frac{(\sigma_{22}+\sigma_{33})^2}{4S_{23}^2} + \frac{\sigma_{23}^2-\sigma_{22}\sigma_{33}}{S_{23}^2} + \frac{\sigma_{12}^2+\sigma_{13}^2}{S_{12}^2} \quad (2)$$

where σ and associated subscripts refer to conventional transverse tensile, compressive or shear stress in the local coordinate system. Y_T and Y_c are the tensile and compressive strengths of the matrix and S and associated subscripts are the shear strengths of the matrix. Depending on the failure mode, the angle of the fracture plane, denoted as α in Fig. 6.9, can also be pre-defined and will align parallel to the local '1' or fibre direction, which is at an angle β to the global 'x' direction.

3.3 Microcrack initiation

Two distinct methods of simulating random microcrack initiation within the cryo-tank, based on methods outlined in [33], are used. These methods have been adapted for use with the tape-laid CF/PEEK material described in Section 2. The first approach is based on the inherent random distribution of the material fracture strength in the form of a continuous probability Weibull distribution, which is volume-adjusted to account for the size effects associated with mesh density of the FE damage models. The two properties required to generate a fracture strength distribution for a given material using this method are the mean fracture strength of the material, $\bar{\sigma}_0$, and a Weibull modulus, m. The transverse tensile strength of the tape-laid CF/PEEK was taken here as the mean fracture strength, which is identified as 41 MPa at ambient temperature. Due to the lack of experimental data in the literature on the material, an inverse identification procedure was adopted to estimate the Weibull modulus of the material. Based on the tensile test geometry described in [33], successive tensile test simulations were performed, iteratively adjusting the Weibull modulus for a prescribed strength distribution until the predicted average bulk transverse stress at failure matched the measured value of 41 MPa. Fig. 10 (a) shows the resulting Weibull fracture strength distribution based on the identified m value of 3.5 for 5,000 elements in an FE mesh. Note that a limited distribution is used in simulations in order to prevent the material from having a transverse strength above 100 MPa, taken as the upper limit of physically realistic values.

The second approach is based on an elemental representation of defects whereby voids are represented via reduced element stiffness, leading to stress concentrations. Voids can be represented by ellipsoids within an element volume (Fig. 10 (b)), whose x, y and z dimensions are based on the values of Table 4. The

voids are randomly distributed throughout the material in the finite element model and act to reduce
element stiffness in accordance with the following:

$$E_1^* = \left(1 - \frac{\pi y z}{4}\right) E_1 \qquad (3)$$

$$E_2^* = \left(1 - \frac{\pi x z}{4}\right) E_2 \qquad (4)$$

$$E_3^* = \left(1 - \frac{\pi x y}{4}\right) E_3 \qquad (5)$$

where E_i^* is the reduced element stiffness, E_1 is the fibre direction modulus and E_2, E_3 are the transverse
moduli.

3.4 Tank damage and permeability

The damage sub-model consists of $^1/_8$ th of the cylindrical portion of the cryo-tank, which corresponds
to a section 100 mm wide as shown in Fig. 6. Symmetry boundary conditions are used to constrain the
sub-model and to ensure accurate response in relation to the full cryo-tank. Although the lay-up consists
of 20 plies, only 15 distinct plies are required due to ply pairing e.g. combining two adjacent 90° plies to
form one thicker ply. A SCZM is defined between each ply. The mesh density for each ply was chosen to
allow at least 5 microcracks per cm of cylinder width or circumference. This crack density corresponds to
the maximum crack density observed in heavily damaged cryogenically cycled CF/PEEK laminates in
[28]. Each model comprises 150,000 3D solid elements, with simulations being performed on twenty-
four 2.4GHz cores on a cluster based at the Irish Centre for High Performance Computing (ICHEC).
Model run-times varied between 36 and 72 hours depending on the level of damage formation. Sequential
thermo-mechanical analyses were required in order to model the transient thermal behaviour shown in
Fig. 5.

Simulations were performed using the two different microcrack initiation methods described in Section
3.3. Volume-adjusted Weibull fracture strengths, generated using the Weibull modulus of 3.5, were
randomly assigned to each element in the FE mesh. A number of the lay-ups of Fig. 7 were modelled
using this method, as shown in Fig. 11.

In accordance with the transverse stress profiles in Fig. 7, significant microcracking was observed in the
[90°₂/±30°/±22°/90°₂/±15°₂]ₛ lay-up, with damage accumulation reaching such a level that the simulation

10

was halted due to the estimated convergence time. The $[90°_2/\pm75°/\pm60°/90°_2/\pm45°_2]_S$ and

$[90°_2/\pm70°/\pm50°/90°_2/\pm30°_2]_S$ lay-ups performed better, with less microcracking at equivalent loading.

However damage reached an unacceptable level before the load step was complete. Delamination

initiation areas can be seen in Fig. 11 for these simulations. The $[90°_2/\pm75°_2/90°_2/\pm60°_2]_S$ lay-up achieved

convergence promptly, with moderate levels of microcracking visible through the tank wall. In order to

investigate damage formation in this lay-up, an additional four simulations were undertaken using the

Weibull method (Fig. 12) and three using the direct defect method (i.e. for more random distributions of

fracture strengths) (Fig. 13). The void dimensions from Table 4 for the QI2 specimen were used for the

direct defect simulation, giving an average void content of between 1.45%, the highest measured by the

3D X-ray CT analysis.

A qualitative analysis of the damage formation shown in Figs. 12 and 13 indicates consistent

microcracking for each method within their respective sample set, with low-to-moderate damage levels

visible in most plies. A quantitative analysis of the average ply-by-ply crack density for each method is

given in Fig. 14. The variation in crack density for the Weibull method mirrors the transverse stress

distribution for the lay-up shown in Fig. 7, with the centre $\pm60°$ plies exhibiting the highest number of

microcracks. It is also worth noting that the average crack densities of the plies on the inner surface of the

tank were higher than their corresponding plies on the outer surface. Although microcracks initiated in

every ply throughout the tank wall, the low crack density of the outer plies meant that no through-

thickness crack networks were detected for any of the five Weibull simulations, implying negligible

permeability for the design. Crack density values taken from the direct defect simulations show the same

microcracking trend for the centre plies. However no microcracks were observed in the hoop or $\pm75°$

plies. This was due to the void induced stress concentrations being of insufficient magnitude to initiate

cracking in these plies, despite the maximum measured void content being used in the simulations. In this

case, the Weibull method can be considered a more thorough approach to damage and permeability

prediction.

4. Conclusions

A combined experimental and numerical method for the prediction of damage and permeability in

internally pressurised linerless cryogenic tape-laid tanks is presented. A detailed characterisation of a tape

–laid CF/PEEK material is presented, with temperature-dependant material properties covering the range

11

from processing to cryogenic temperatures. Optical micrography and 3D X-ray CT were used to investigate the defect content of the material as well as damage due to cryogenic cycling. Void content of the tape-laid material was found to be an order of magnitude higher than for comparable autoclave processed material, although similar trends in void morphology were observed. Transverse microcracks were also present throughout the test specimens post-cycling.

A detailed tank design, based on reducing the transverse stress throughout the tank wall, was developed. Unlike lay-ups typically used for COPVs, a combination of hoop and high-angle helical plies were found to be most efficient at reducing transverse stress levels due to combined thermo-mechanical loading. A sub-model of the cryo-tank was developed to predict intra- and inter-ply damage formation based on a novel XFEM-SCZM methodology. The material properties and defect distributions of the tape-laid material were used as inputs for the model. Two methods of modelling microcrack initiation were employed: a Weibull distribution of fracture strengths method and a void-based stiffness reduction method. Several lay-up variations were tested using the modelling technique. The optimised high-angle helical tank was shown to be least susceptible to through-thickness microcrack formation and hence cryogen leakage.

5. References

[1] Madhavi M., Rao K.V.J. & Rao K.N. Design and analysis of filament wound composite pressure vessel with integrated-end domes. *Defence Science Journal*, **59**(1), 73-81, 2009.

[2] Tam W.H., Griffin P.S. & Jackson A.C. Design and manufacture of a composite overwrapped pressurant tank assembly. 38th AIAA/ASME/SAE/ASEE Joint Propulsion Conference & Exhibit, Indiana, USA, 7-10th July, 2002.

[3] Kim E., Lee I. & Hwang T.K. Impact response and damage analysis of composite overwrapped pressure vessels. 52nd AIAA/ASME/ASCE/AHS/ASC Structures Dynamics and Materials Conference, Colorado, USA, 4-7th April, 2011.

[4] Mian H.H., Wang G., Dar U.A. & Zhang W. Optimization of composite materials system and lay-up to achieve minimum weight pressure vessel. *Applied Composite Materials*, **20**(5), 873-889, 2013.

[5] Grimsley B.W., Cano R.J., Norman J.J., Loos A.C. & McMahon W.M. Hybrid Composites for LH2 Fuel Tank Structure, NASA Langley Research Center, Virginia, USA, 2001.

[6] Ju J., Pickle B.D., Morgan R.J., & Reddy J.N. An initial and progressive failure analysis for cryogenic composite fuel tank design. *Journal of Composite Materials*, **41**(21), 2545-2568, 2007.

[7] Kang S., Kim M., Park S., Kim C. & Kong C. Damage analysis of a type 3 cryogenic propellant tank after LN$_2$ storage test. *Journal of Composite Materials*, **42**(10), 975-992, 2008.

[8] Sonmez F.O., Hahn H.T. & Akbulut M. Analysis of process-induced residual stresses in tape placement. *Journal of Thermoplastic Composite Materials*, **15**(6), 525-544, 2002.

[9] Croft K., Lessard L., Pasini D., Hojjati M., Chen J. & Yousefpour A. Experimental study of the effect of automated fiber placement induced defects on performance of composite laminates. *Composites Part A: Applied Science and Manufacturing*, **42**(5), 484-491, 2011.

[10] Aoki T., Ishikawa T., Kumazawa H. & Morino Y. Mechanical Behaviour of CF/Polymer Composite Laminates under Cryogenic Environment. Proceedings of the 12th International Conference on Composite Materials, Paris, France, 1997.

[11] Yoon H. & Takahashi K. Mode I interlaminar fracture toughness of commingled carbon fibre/PEEK composites. *Journal of Materials Science*, **28**(7), 1849-1855, 1993.

[12] Stokes-Griffin C. M., Matuszyk T. I., Compston p. & Cardew-Hall M.J.. Modelling the automated tape placement of thermoplastic composites with in-situ consolidation. *Sustainable Automotive Technologies*, 61-68, 2012.

[13] Kilroy J.P., Ó Brádaigh C.M. & Semprimoschnig C.O.A. Mechanical and physical evaluation of new carbon fibre/peek composites for space applications. S.A.M.P.E Journal, **44**(3), 22-34, 2008.

[14] Comer A.J., Ray D., Obande W.O., Jones D., Rosca I, O' Higgins R.M. & McCarthy M.A. Mechanical characterisation of carbon fibre–PEEK manufactured by laser-assisted automated-tape-placement and autoclave. *Composites Part A: Applied Science and Manufacturing*, **68**, 10-20, 2015.

13

[15] Jeronimidis G. & Parkyn A.T. Residual Stresses in Carbon Fibre-Thermoplastic Matrix Laminates. *Journal of Composite Materials*, **22**(5), 401-415, 1988.

[16] Kumazawa H. & Whitcomb J. Numerical Modelling of Gas Leakage through Damaged Composite Laminates. *Journal of Composite Materials*, **42**(16), 1619-1638, 2008.

[17] Bois C., Malenfant J.C., Wahl J.C. & Danis M. A multiscale damage and crack opening model for the prediction of flow path in laminated composite. *Composites Science and Technology*, **97**, 81-89, 2014.

[18] Kam T.Y., Liu Y.W. & Lee F.T. First-ply failure strength of laminated composite pressure vessels. *Composite Structures*, **38**(1-4), 65-70, 1997.

[19] Chang R.R. Experimental and theoretical analyses of first-ply failure of laminated composite pressure vessels. *Composite Structures*, **49**(2), 237-243, 2000.

[20] Mallick K., Cronin J., Ryan K., Arzberger S., Munshi N., Paul C. & Welsh J.S. An integrated systematic approach to linerless composite tank development. 46th AIAA/ASME/ASCE/AHS/ASC Structures, Structural Dynamics, and Materials Conference, Texas, USA, 18-21st April, 2005.

[21] Ryan K., Cronin J., Arzberger S., Mallick K., Munshi N., Yazdani F., Kallmeyer A., Arritt B. & Welsh J.S. Prediction of pressure cycle induced microcrack damage in linerless composite tanks. 47th AIAA/ASME/ASCE/AHS/ASC Structures, Structural Dynamics, and Materials Conference, Rhode Island, USA, 1-4th May, 2006.

[22] [3]Suprem Victrex IM7 , The Irish Centre for Composites Research (ICOMP), private communication, 2015.

[23] [1]Suprem Victrex AS4, [4]Suprem Victrex IM7, ÉireComposites Teo, private communication, 2012

[24] [2]Cytec APC-2/IM7, Cytec Engineered Materials. APC-2 PEEK Thermoplastic Polymer Technical Data Sheet. www.cytec.com, 2012.

[25] Wang C. & Sun C.T. Thermoelastic behaviour of PEEK thermoplastic composite during cooling from forming temperatures. *Journal of Composite Materials*, **31**(22), 2230-2248, 1997.

[26] Melo J.D.D & Radford D.W. Elastic properties of peek/IM7 related to temperature. Journal of Reinforced Plastics and Composites, 22(12), 1123-1139, 2003.

[27] Holmes S.T. & Gillespie J.W. Thermal analysis for resistance welding of large-scale thermoplastic composite joints. *Journal of Reinforced Plastics and Composites*, **12**(6), 723-736, 1993.

[28] Grogan D.M., Leen S.B, Semprimoschnig C.O.A. & Ó Brádaigh C.M. Damage characterisation of cryogenically cycled carbon fibre/PEEK laminates. *Composites Part A: Applied Science and Manufacturing*, **66**, 237-250, 2014.

[29] Murray B.R., Leen S.B. & Ó Brádaigh C.M. Void distributions and permeability prediction for rotationally moulded polymers. *Proceedings of the Institution of Mechanical Engineers, Part L: Journal of Materials: Design and Applications*, 2014. DOI: 10.1177/1464420714525135.

[30] Akula V.M.K & Schubert M.K. Analysis of debonding of filament wound composite pressure vessels. *Proceedings of the American Society of Composites – 28th Technical Conference*, 2013.

[31] Tam W., Hersh M. & Ballinger I. H. Hybrid propellant tanks for spacecraft and launch vehicles. 39th AIAA Propulsion Conference, Alabama, USA, 21st July, 2003.

[32] Grogan D.M., Leen S.B & Ó Brádaigh C.M. An XFEM-based methodology for fatigue delamination and permeability of composites. *Composite Structures*, **107**, 205-218, 2014.

[33] Grogan D.M., Ó Brádaigh C.M. & Leen S.B. A combined XFEM and cohesive zone model for composite laminate microcracking and permeability. *Composite Structures*, **120**, 246-261, 2015.

[34] Feerick E.M., Liu X. & McGarry P. Anisotropic mode-dependent damage of cortical bone using the extended finite element method (XFEM). *Journal of the Mechanical Behaviour of Biomedical Materials*, **20**, 77-89, 2013.

[35] Hashin Z. Failure criteria for unidirectional fiber composites. *Journal of Applied Mechanics*, **47**(2), 329-334, 1980.

Figure captions

Figure 1 *3D X-ray-CT scan of voids present in tape-laid UD1 (top) and hoop CF/PEEK specimens (bottom). (Where the x direction is the fibre direction, y is transverse to the fibre direction and z is the thickness direction).*

Figure 2 *(a) Distribution of void volumes below 0.1 mm³ arranged from highest to lowest measured using 3D X-ray CT for tape-laid unidirectional (UD1) and quasi-isotropic CF/PEEK specimens (QI1). (b) Bar chart showing the frequency of voids within a given volume range. (c) Relationship between the sphericity and the equivalent radius of voids from specimens UD1 and QI1.*

Figure 3 *An optical micrograph of gaps, a surface microcrack and voids in the tape-laid CF/PEEK specimen QI2, as processed (top), a micrograph of a gap and two transverse microcracks present in specimen QI2 after exposure to a single cryogenic cycle (left) and rendered 3D X-ray CT scan of microcracking and gaps in the same specimen (right).*

Figure 4 (a) *Ply level microcracking detected using micrographs of QI1 and QI2 after cryogenic cycling. Gaps are also included. (b) Crack opening displacement and gap width measurement from cycled specimens. Ply groups 1 - 9 refer to symmetric ply pairs i.e. ply group 1 comprises the outer 45° plies.*

Figure 5 *Plot of temperature on the inner and outer surfaces of the tank wall due to the two-stage cooling related to the processing and fuelling windows. The increase in internal tank pressure is also shown.*

Figure 6 *Schematic showing the location of the cylindrical sub-model in relation to the full cryo-tank. Tank design is focused on this sub-region.*

Figure 7 *Transverse stress distributions through the cylindrical portion of the tank wall for several lay-up variations under the loading described in Fig. 5. The numbers in the legend refer to the angles $\pm \boldsymbol{\theta}°$ in the general 20-ply lay-up $[90°_2/\pm \theta°/\pm \theta °/90°_2/\pm \theta°_2]_S$. QI refers to the test specimen lay-up $[45°/-45°/90°/0°/90°/0°/90°/0°/90°]_S$.*

Figure 8 *The combined XFEM-SCZM method facilitates prediction of microcracking and delamination in large scale structures such as the cylindrical sub-model of the cryo-tank shown above.*

Figure 9 *Schematic showing the microcrack morphology related to tensile, compressive and shear loading in a two-element model. Oblique fracture planes are orientated at a prescribed angle $\boldsymbol{\alpha}$ (i.e 45° for transverse compression) and are parallel to the ply fibre angle $\boldsymbol{\beta}$.*

Figure 10 *(a) De-limited and limited Weibull distributions used in modelling. The element fracture strengths are ordered smallest to largest. (b) Schematic of an air void within an element. The reduction in*

16

element stiffness is based on the dimensions of the void as measured using 3D X-ray CT and forms the basis of the direct defect method.

Figure 11 *Comparison of through-thickness damage formation from the outer to the inner surface of the tank for several lay-ups showing XFEM microcracking and intensity of inter-laminar forces (SCZM) (red – high; blue – low).*

Figure 12 *Damage formation in the remaining four Weibull damage models for the $[90°_2/\pm75°_2/90°_2/\pm60°_2]_S$ lay-up.*

Figure 13 *Damage profiles for three realisations of the $[90°_2/\pm75°_2/90°_2/\pm60°_2]_S$ lay-up obtained using the direct defect method, each with an average void content of approximately 1.45%.*

Figure 14 *Comparison of average crack densities for each ply of the $[90°_2/\pm75°_2/90°_2/\pm60°_2]_S$ cryo-tank predicted by the Weibull and direct defects modelling methods. Ply 1 is on the inner surface of the tank.*

Table captions

Table 1 *Measured temperature-dependant mechanical and fracture properties of CF/PEEK materials. E and G are the elastic and shear moduli, TTS and TCS are the transverse tensile and compressive strengths, IPSS and ILSS are the in-plane and inter-laminar shear strengths, G_{IC} and G_{IIC} are Mode I and Mode II fracture toughness. The subscripts 1 and 2 refer to the longitudinal and transverse directions. [1]Suprem Victrex AS4 [23], [2]Cytec APC-2/IM7 [24], [3]Suprem Victrex IM7 [22], [4]Suprem Victrex IM7 [23].*

Table 2 *Measured temperature-dependant mechanical and thermal properties of CF/PEEK materials. E and G are the elastic and shear moduli, ν is Poisson's ratio, ρ is density, SHC is the specific heat capacity, α and k are the thermal expansion coefficients and conductivities. The subscripts 1 and 2 refer to the longitudinal and transverse directions. [1]APC-2/AS4 adapted from [25], [2]PEEK/IM7 adapted from [26], [3]APC-2/AS4 adapted from [27].*

Table 3 *Interpolated temperature-dependant material properties for tape-laid Suprem IM7 based on the measured properties in Tables 1 and 2.*

Table 4 *Mean and standard deviation of the x, y and z dimensions of voids in unidirectional (UD1, UD2), hoop and quasi-isotropic (QI1, QI2) tape-laid CF/PEEK specimens measured using 3D X-ray CT. Void volume content is also provided, where possible. *Indicates gaps included in void content.*
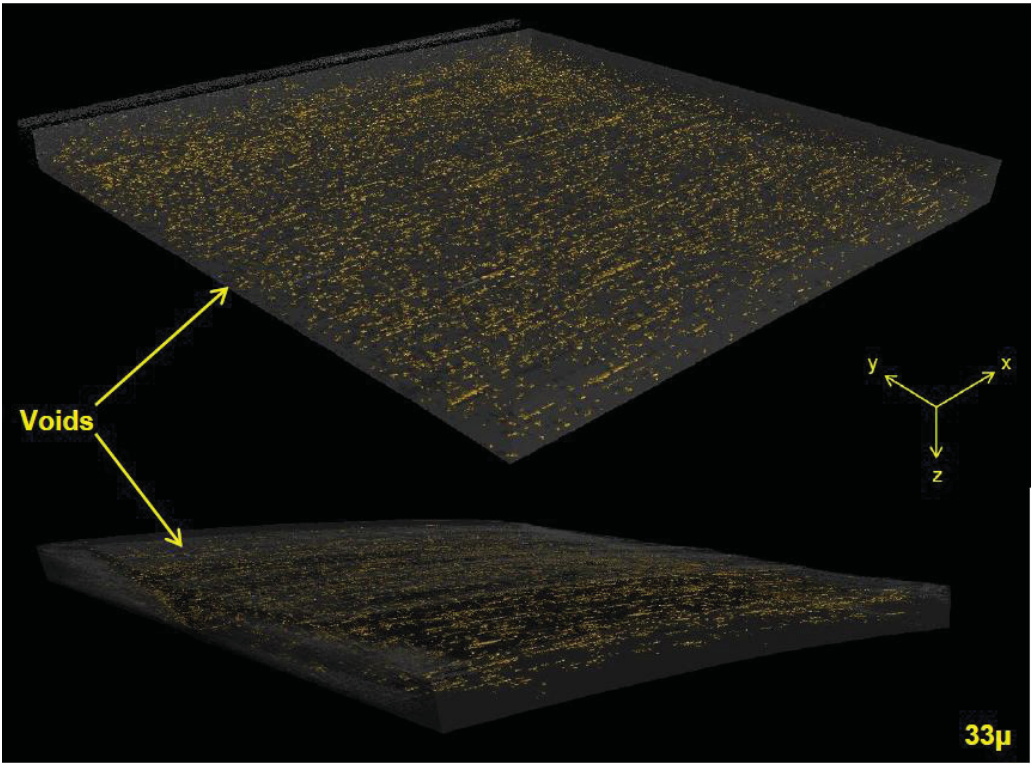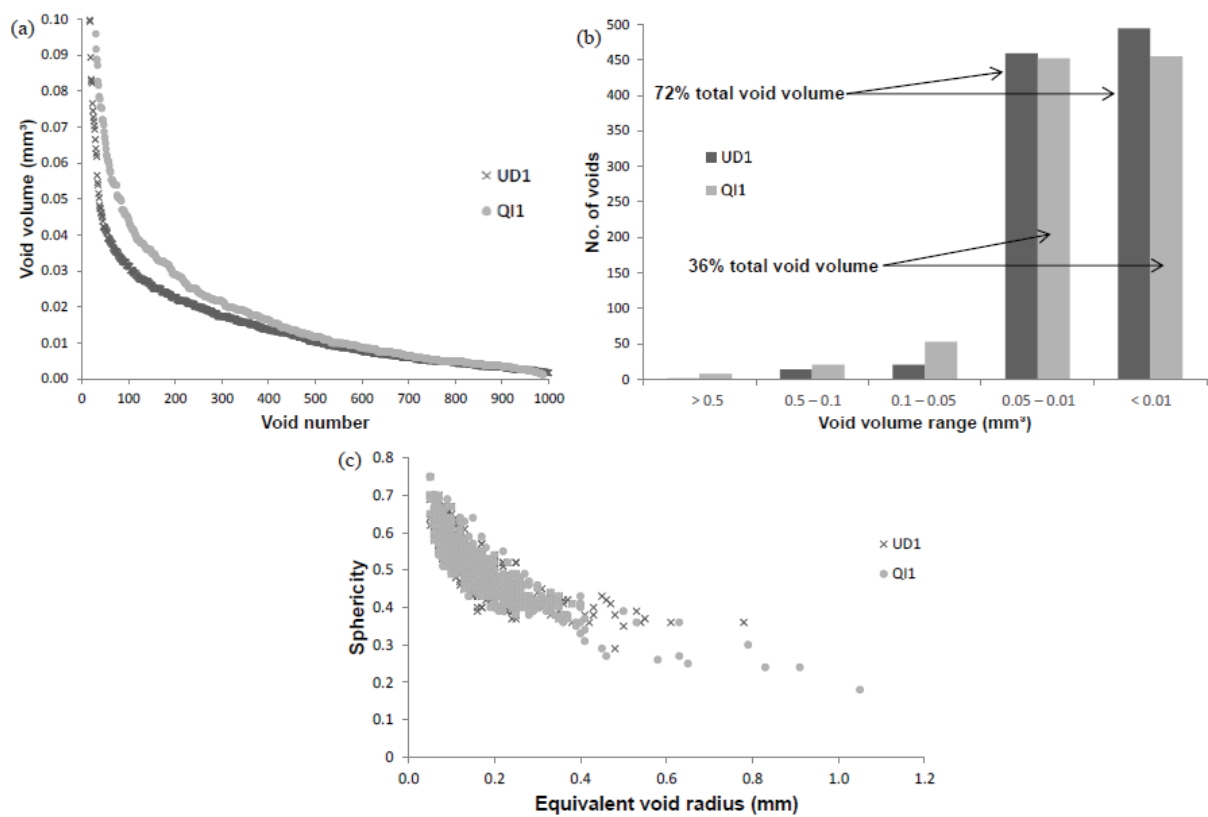
Figure(s)
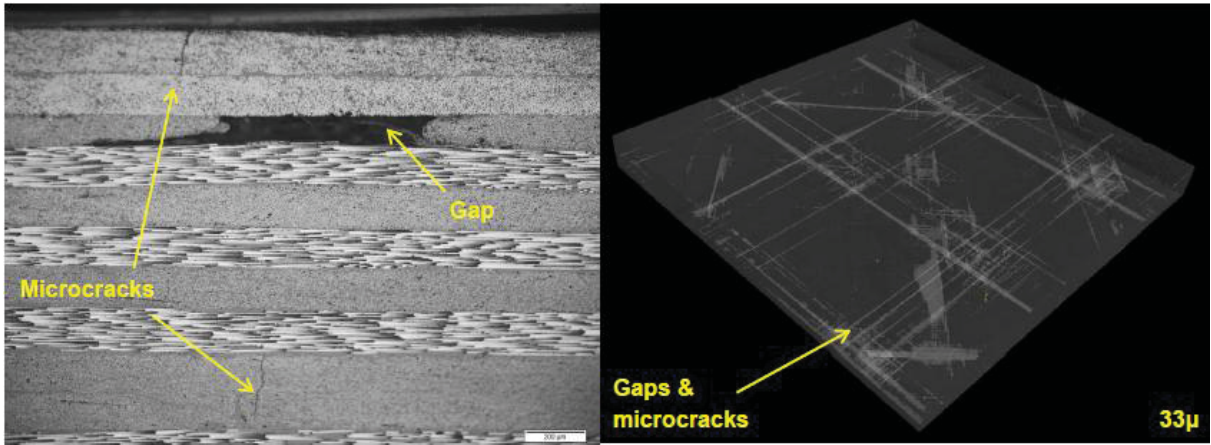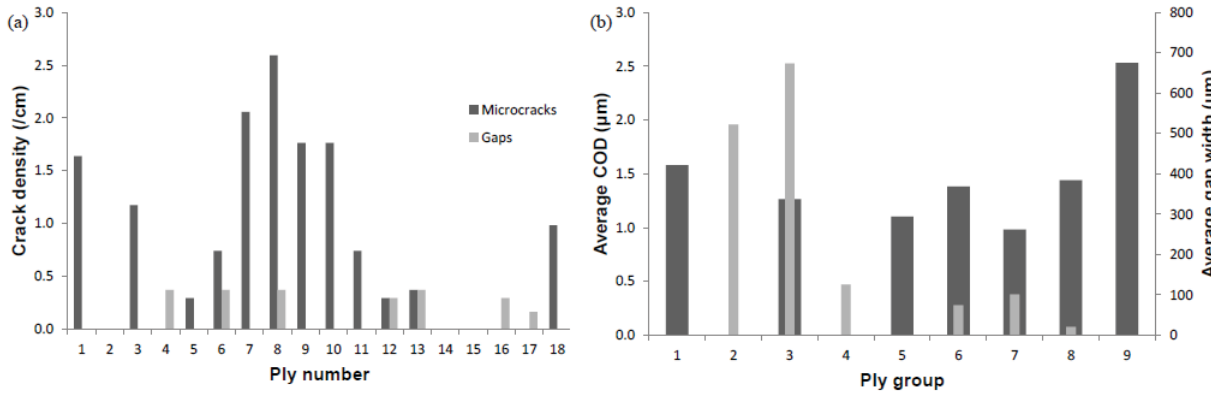

Figure 1

Figure 2

Figure(s)

Figure 3

Figure 4

Figure(s)
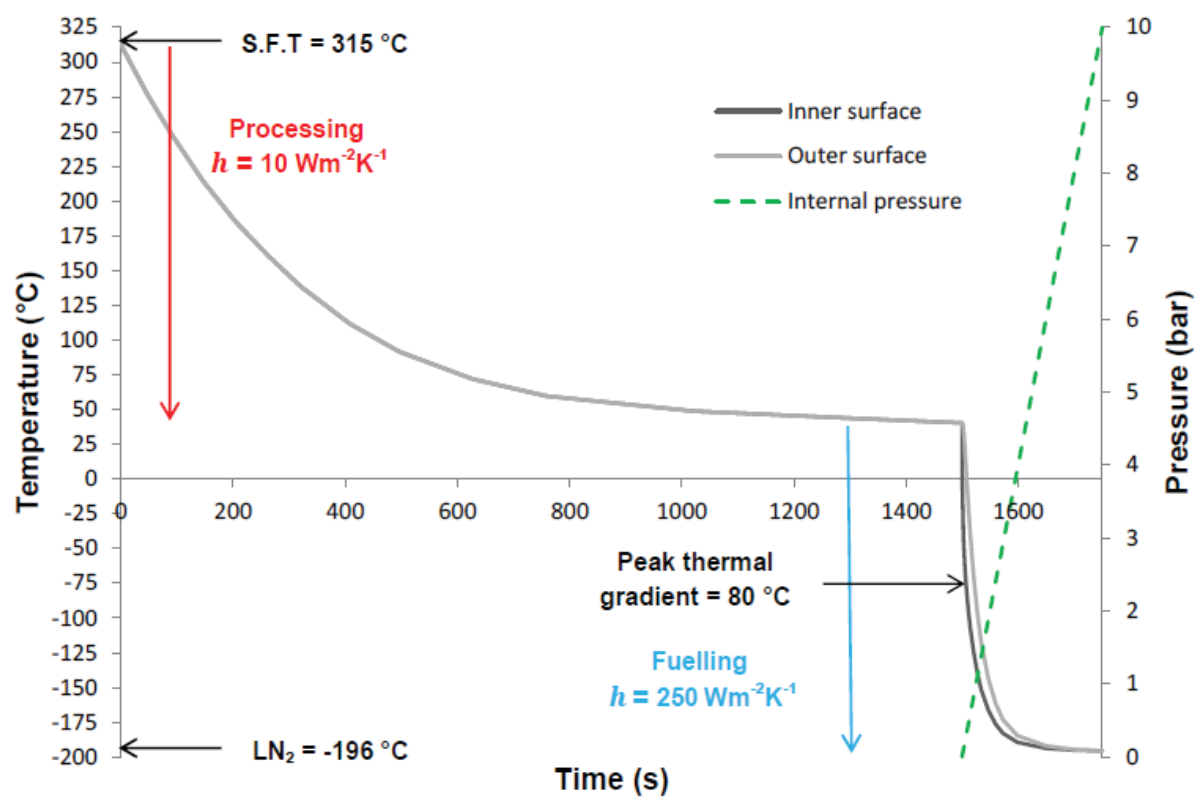
Figure 5
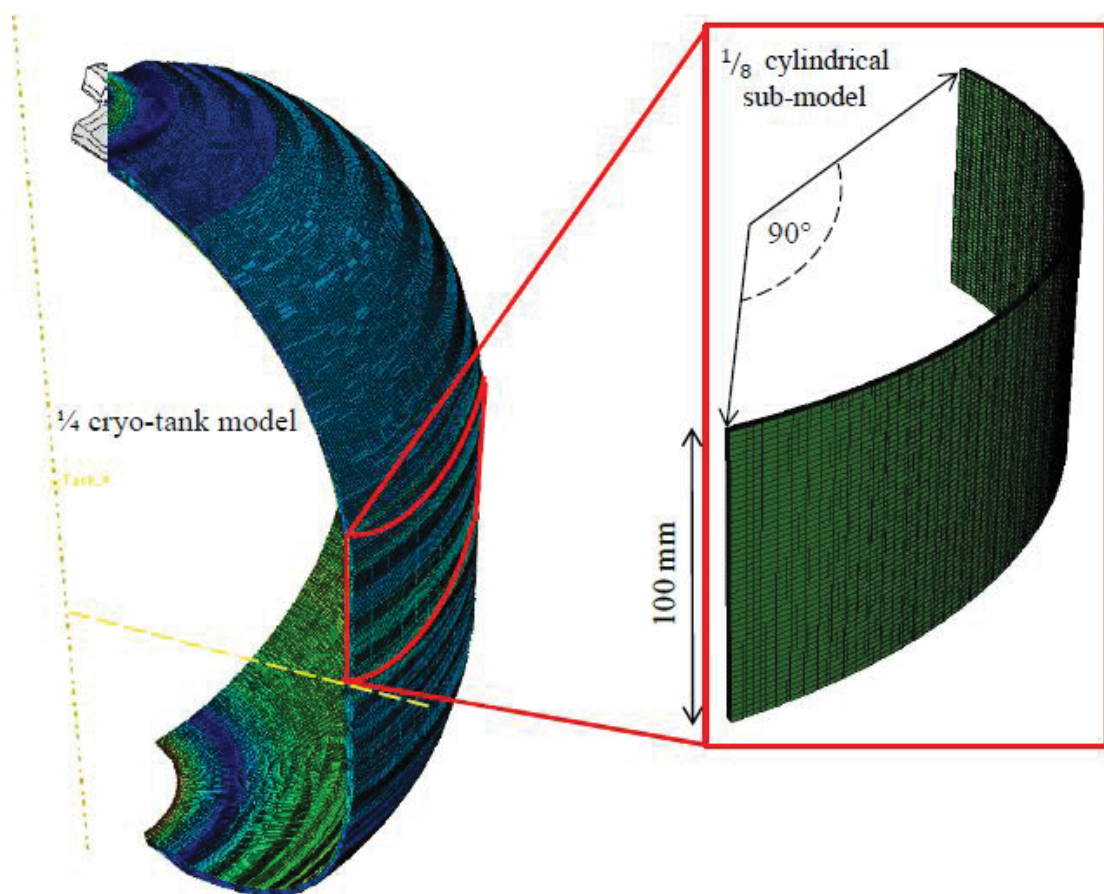
Figure 6

Figure 7

Figure 8

Transverse tension

Longitudinal shear

Global

Transverse compression

Transverse shear

Microcrack
surface

Ply
thickness

α

β Fibre
orientation

Local

Fracture plane angle

Figure 9

(a)

Weibull modulus m from
virtual tensile testing

× De-limited Weibull

— Limited Weibull

(b)

Void

Element

Figure 10

$[90°_2/\pm30°/\pm22°/90°_2/\pm15°_2]_s$

$[90°_2/\pm75°/\pm60°/90°_2/\pm45°_2]_s$

XFEM microcracking

$[90°_2/\pm70°/\pm50°/90°_2/\pm30°_2]_s$

$[90°_2/\pm75°_2/90°_2/\pm60°_2]_s$

Delamination initiation

Figure 11

XFEM + SCZM

XFEM
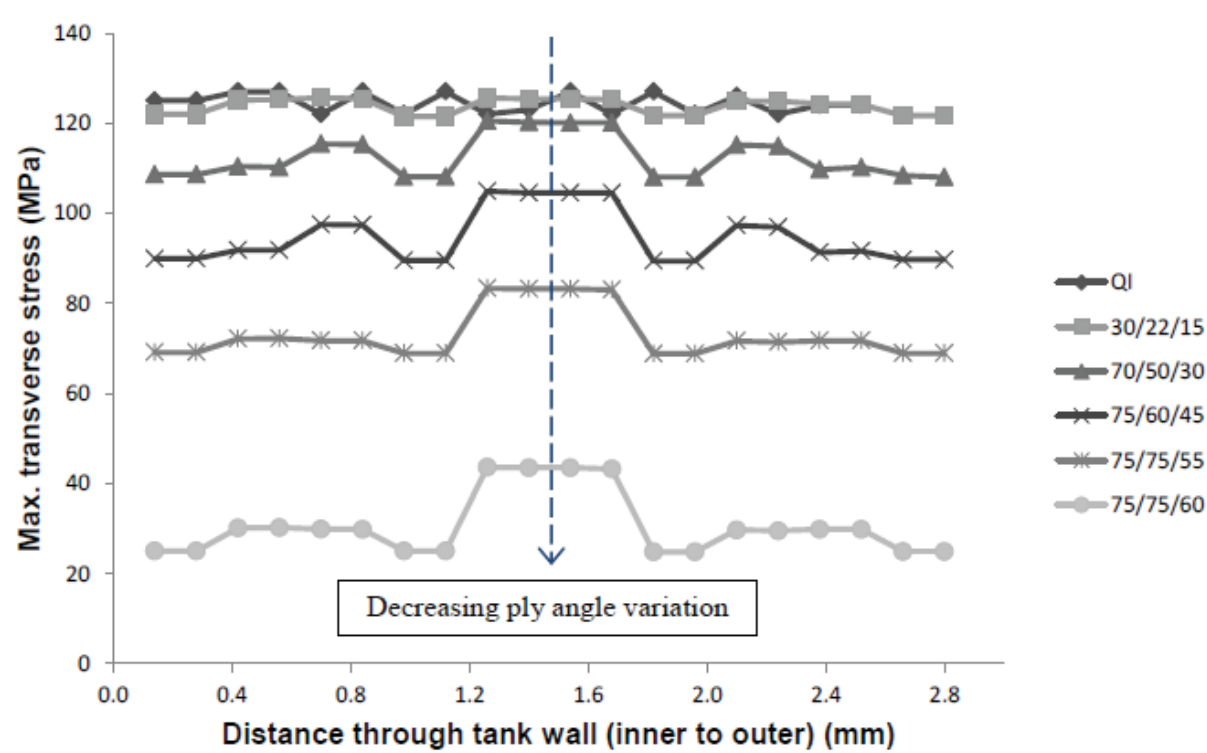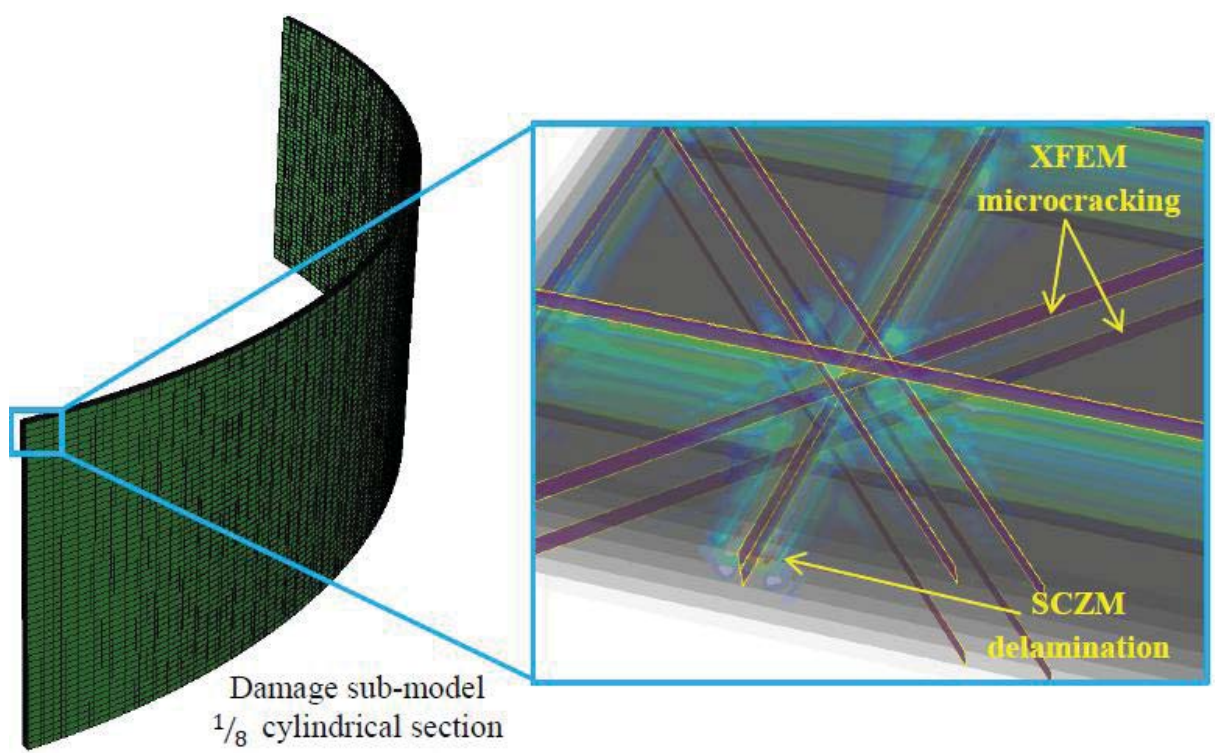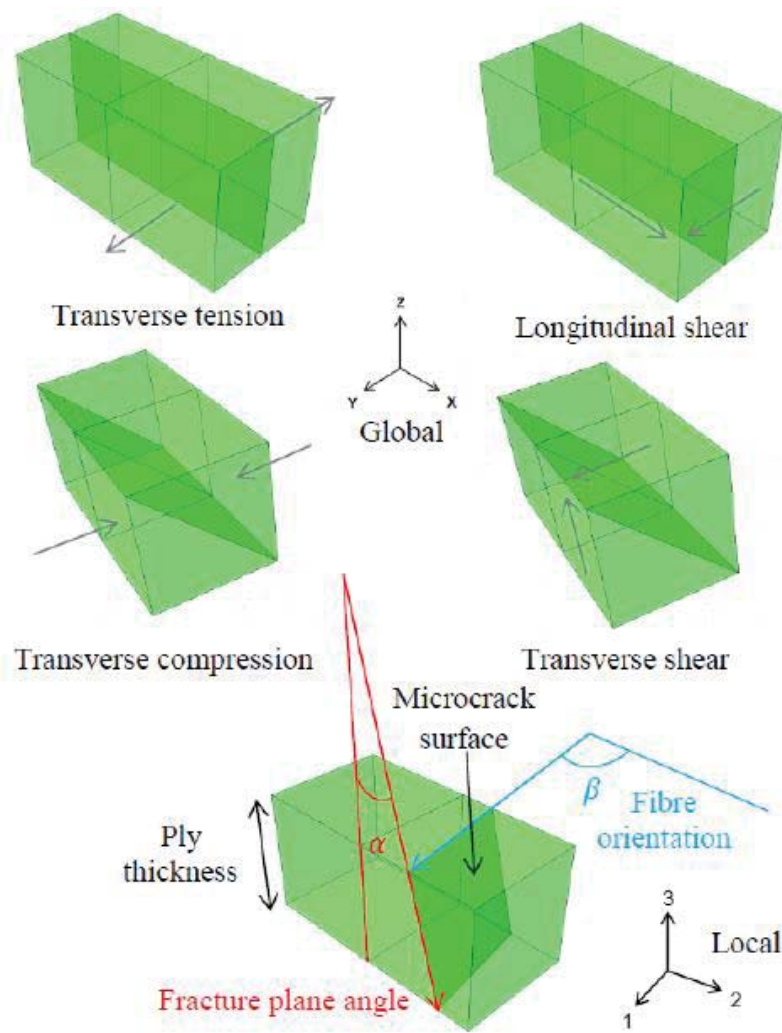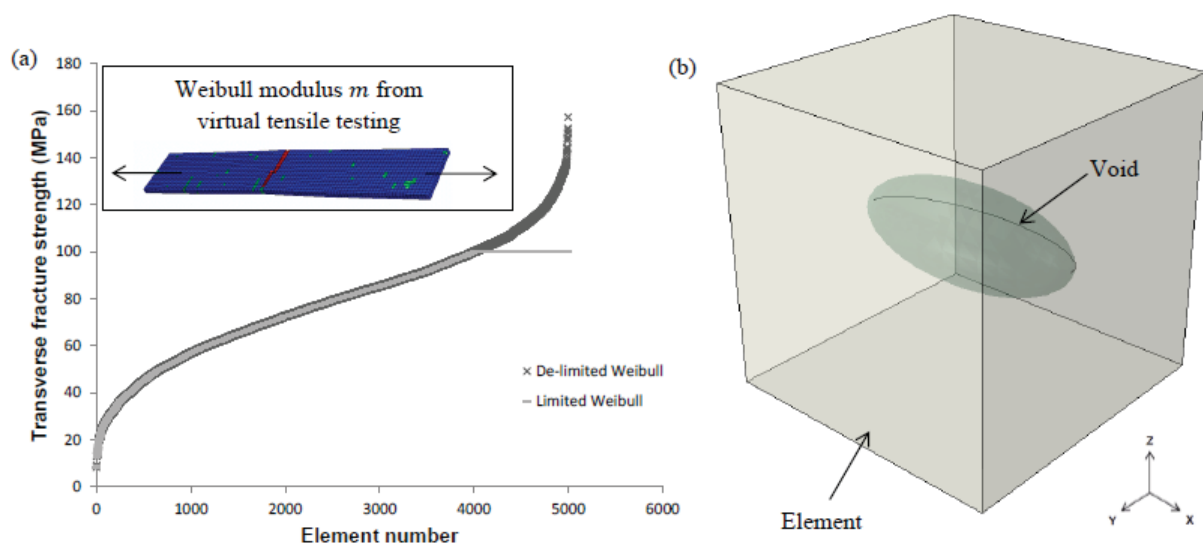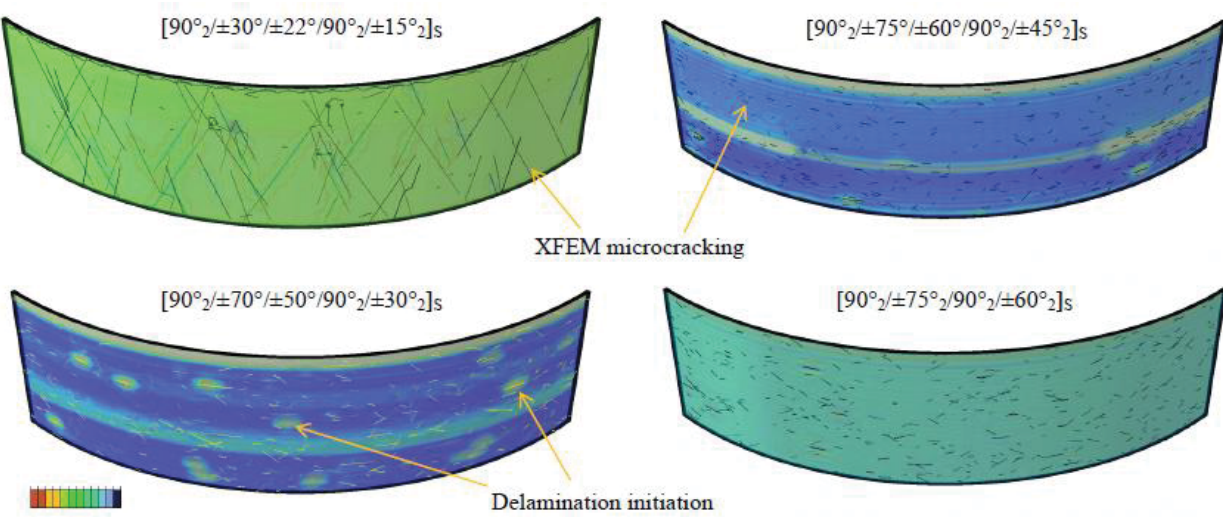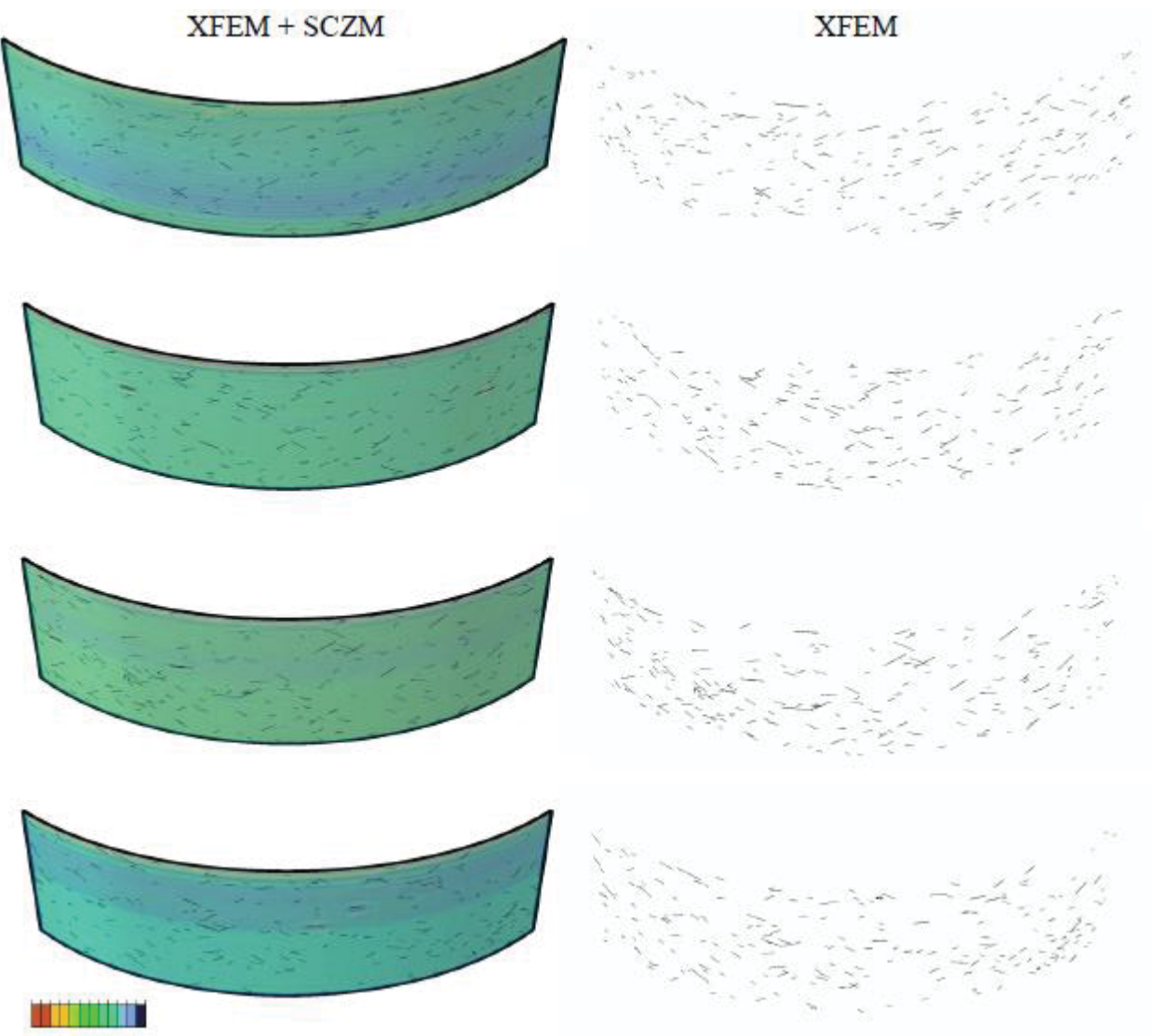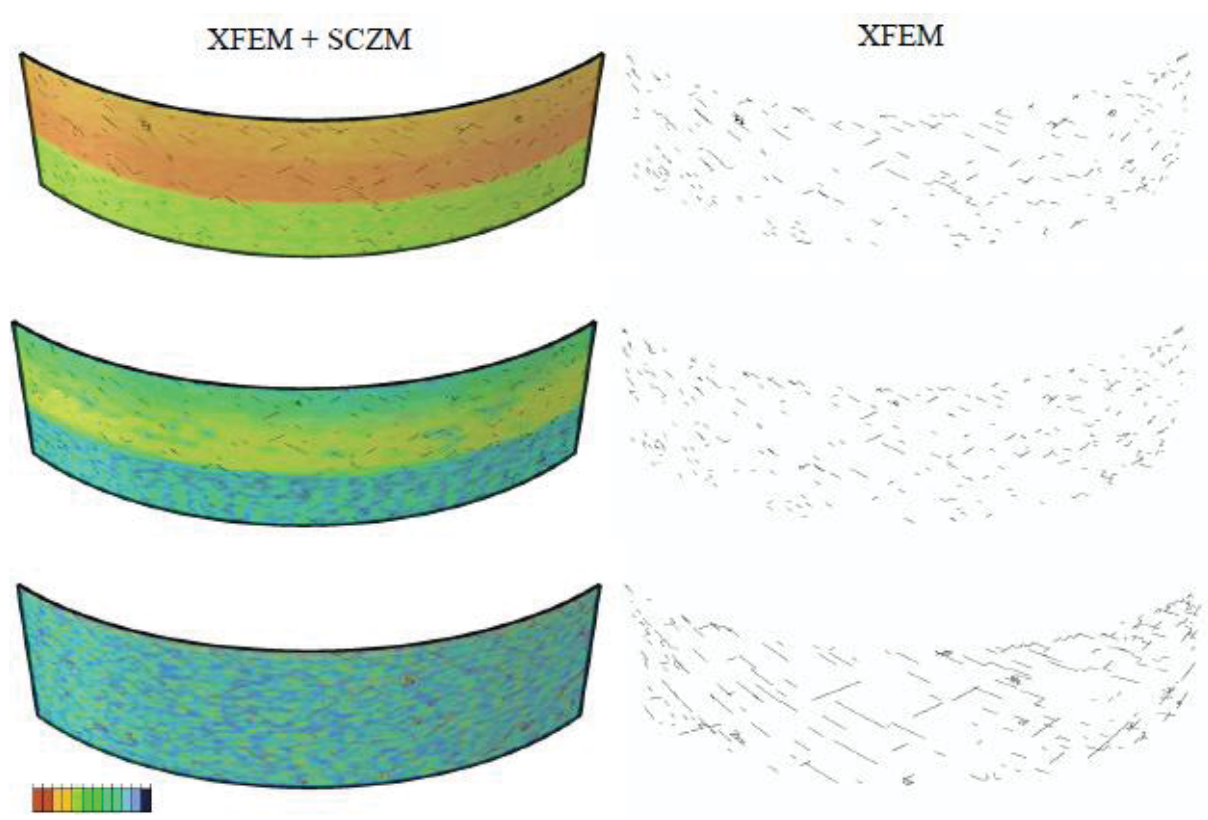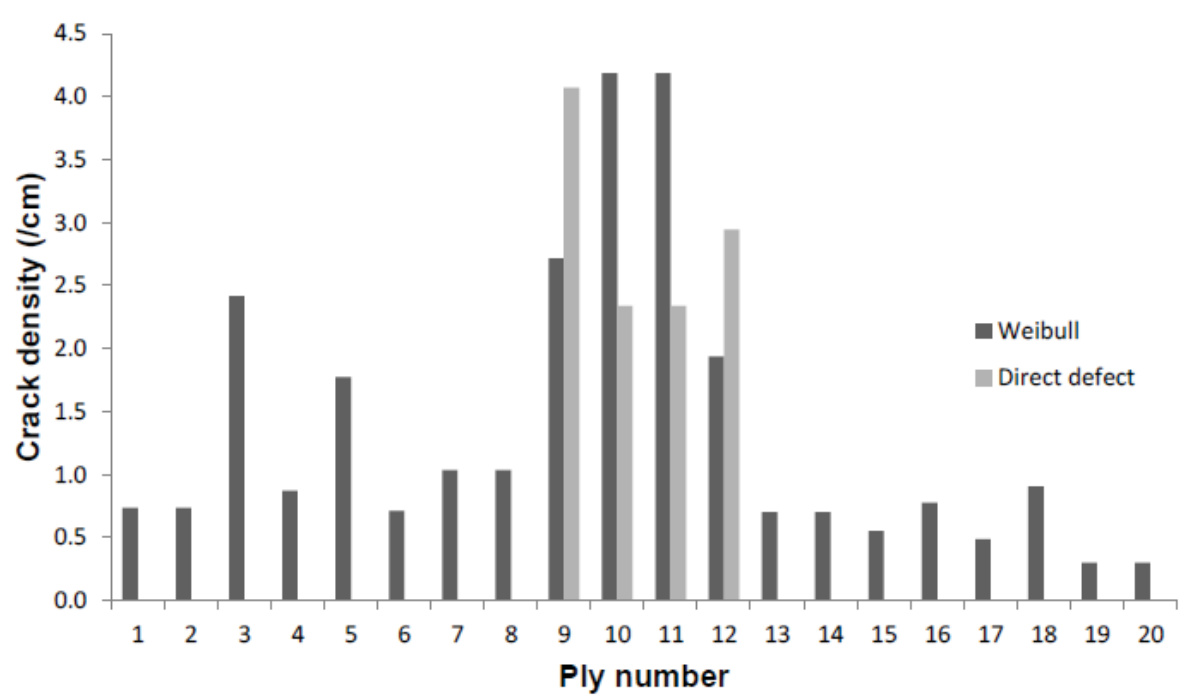
Figure 12

Figure 13

Figure 14

Table(s)

Temp. (°C)	E_1 (GPa)	E_2 (GPa)	G_{12} (GPa)	TTS (MPa)	TCS (MPa)	IPSS (MPa)	ILSS (MPa)	G_{IC} (J/m²)	G_{IIC} (J/m²)
-196	[1]141	-	-	[1]51	-	[1]81	[1]106	-	-
-70	-	-	-	[1]63	-	[1]104	[1]116	-	-
-55	[2]172	[2]11	[2]5.9	-	-	-	-	[2]1600	[2]2100
25	[3]155.0	[3]8.6	[3]4.00	[3]41	[3]163	[3]80	[3]98	[3]1910	[4]1355
125	-	-	-	[1]48	-	[1]75	-	-	-

Temp. (°C)	[1]E_1 (GPa)	[1]E_2 (GPa)	[1]G_{12} (GPa)	[2]ν_{12}	[3]ρ (kg/m³)	[3]SHC (j/kg.K)	[3]α_1 (10⁻⁶/K)	[3]α_2 (10⁻⁶/K)	[3]k_1 (W/m.K)	[3]k_2 (W/m.K)³
25	134	10.3	6.00	0.32	1598	930	0.2	28.8	3.5	0.4
50	134	10.3	6.00	0.32	1598	930	0.2	29.4	4.6	0.5
75	134	9.6	5.43	0.34	1598	930	0.3	30.0	4.9	0.6
100	134	9.6	5.43	0.35	1593	1040	0.3	31.0	5.1	0.6
125	134	8.3	4.86	0.36	1593	1040	0.4	32.4	5.5	0.6
150	131	8.3	4.86	0.37	1586	1260	0.4	40.0	5.9	0.7
175	131	4.5	2.51	-	1586	1260	0.5	47.7	5.9	0.7
200	130	4.3	2.16	-	1575	1300	0.5	50.0	5.9	0.7
225	130	4.3	2.16	-	1575	1300	0.6	60.0	6.0	0.7
250	129	3.6	0.95	-	1563	1400	0.7	70.0	6.1	0.7
275	130	3.6	0.95	-	1563	1400	0.8	80.0	6.4	0.7
300	130	1.7	0.53	-	1551	1550	0.9	90.0	6.7	0.8
315	128	0.6	0.23	-	1551	1550	1.0	108.0	6.7	0.8

Temp. (°C)	E_1 (GPa)	E_2 (GPa)	G_{12} (GPa)	v_{12}	ρ (kg/m³)	SHC (j/kg.K)	α_1 (10^{-6}/K)	α_2 (10^{-6}/K)	k_1 (W/m.K)	k_2 (W/m.K)	TTS (MPa)	TCS (MPa)	IPSS (MPa)	ILSS (MPa)	G_{Ic} (J/m²)	G_{IIc} (J/m²)
-196	152.0	-	-	-	-	-	-	-	-	-	39	-	74	121	-	-
-70	-	-	-	-	-	-	0.0	24.7	-	-	47	-	95	133	-	-
-55	155.0	9.5	4.40	-	-	-	-	-	-	-	-	-	-	-	1340	1890
25	155.0	8.6	4.00	0.32	1598	930	0.2	28.8	3.5	0.4	41	163	80	98	1910	1710
50	155.0	8.6	4.00	0.32	1598	930	0.2	29.4	4.6	0.5	-	-	-	-	-	-
75	155.0	8.0	3.62	0.34	1598	930	0.3	30.0	4.9	0.6	-	-	-	-	-	-
100	155.0	8.0	3.62	0.35	1593	1040	0.3	31.0	5.1	0.6	-	-	-	-	-	-
125	155.0	6.9	3.24	0.36	1593	1040	0.4	32.4	5.5	0.6	36	-	69	74	-	-
150	151.5	6.9	3.24	0.37	1586	1260	0.4	40.0	5.9	0.7	-	-	-	-	-	-
175	151.5	3.8	1.67	0.37	1586	1260	0.5	47.7	5.9	0.7	-	-	-	-	-	-
200	150.4	3.6	1.44	-	1575	1300	0.5	50.0	5.9	0.7	-	-	-	-	-	-
225	150.4	3.6	1.44	-	1575	1300	0.6	60.0	6.0	0.7	-	-	-	-	-	-
250	149.2	3.0	0.63	-	1563	1400	0.7	70.0	6.1	0.7	-	-	-	-	-	-
275	150.4	3.0	0.63	-	1563	1400	0.8	80.0	6.4	0.7	-	-	-	-	-	-
300	150.4	1.4	0.35	-	1551	1550	0.9	90.0	6.7	0.8	-	-	-	-	-	-
315	148.0	0.5	0.16	-	1551	1550	1.0	108.0	6.7	0.8	-	-	-	-	-	-

Table(s)

Specimen	x̄ (mm)	σ(x) (mm)	ȳ (mm)	σ(y) (mm)	z̄ (mm)	σ(z) (mm)	Void (%)
UD1	0.265	0.169	0.168	0.073	0.087	0.045	0.26
UD2	0.280	0.183	0.171	0.075	0.093	0.041	0.33
Hoop	0.244	0.185	0.193	0.131	0.098	0.066	0.22
QI1	0.281	0.208	0.196	0.161	0.083	0.039	0.69
QI2	0.264	0.143	0.190	0.150	0.086	0.079	N/A
QI2*	0.526	1.117	0.333	1.418	0.106	0.135	1.45